

Chapter 2

Ultrasound-Powered Micro-/Nanorobots: Fundamentals and Biomedical Applications



Liqiang Ren, Fernando Soto, Luyang Huang, and Wei Wang

2.1 Introduction

A micro-/nanorobot is a small, functional device that moves, senses, and operates at a micro- or nanoscale. As this book aptly illustrates, plenty of approaches have been developed to synthesize and power micro-/nanorobots, each with a unique strategy and emphasis. Prominent examples include, on the small side, molecular machines that change configurations under external cues [1, 2], and, on the large side, MEMS/NMES devices that trap cells and inject chemicals [3, 4]. The current chapter, however, deals with the type that is more commonly referred to as micro-/nanomotors, synthetic microswimmers, or colloidal motors that are untethered and swim autonomously in a liquid environment [5, 6]. They do so by harvesting energy stored in their environments, in the form of chemical, electromagnetic, light, heat, and sound energy, the last of which will be the focus of this chapter.

However, before we expand on ultrasound-powered micro-/nanorobots, let us first provide a brief background to set the stage. Micro-/nanorobots, or micro-/nanomotors to be more specific, have been around for roughly two decades, starting from the pioneering discoveries in the early twenty-first century by groups at Penn State and University of Toronto [7, 8], which reported that bimetallic microrods are able to self-propel in aqueous solutions of hydrogen peroxide (H_2O_2). This was the first discovery of synthetic materials that move like living microorganisms and has thus

L. Ren

Department of Engineering Science and Mechanics, The Pennsylvania State University,
University Park, PA, USA

F. Soto

School of Medicine, Stanford University, Palo Alto, CA, USA

L. Huang · W. Wang (✉)

School of Materials Science and Engineering, Harbin Institute of Technology (Shenzhen),
Shenzhen, Guangdong, China

e-mail: weiwangsz@hit.edu.cn

sparked wide interests and intense research efforts in the years that followed (reviewed by other chapters in this book). Ever since this early discovery, the research interest has been in two directions. On the one hand, micro-/nanomotors are envisioned as prototype microrobots for a variety of fascinating operations, such as minimally invasive surgeries [9, 10], biomedical sensing [11, 12], environmental remediation [13–15], and micro-assembly [16–18]. On the other hand, soft matter physicists see micro-/nanomotors as useful model systems in the studies of active matter [19, 20], a physical concept that encompasses anything that self-propels and exhibits collective behaviors. It is these two branches of research, one practical and one fundamental, that drive most of micro-/nanomotor research today.

For either purpose, the power source is one of the key elements in the design of a micro/nanomotor, together with the capability to control, and the integration of useful functionalities. Limited by the physics operating at micro- and nanoscale, in particular Brownian motion and a viscous medium (i.e., low Reynolds number) [21], many classical, inertia-based methods to power macroscopic objects fail for micro-/nanomotors, where surface effects dominate [22]. As a result, the majority of propulsion mechanisms for micro-/nanomotors circumvent the so-called scallop theorem by exploiting the interesting chemistry and physics at the particle-liquid interface. For example, a major category of micro-/nanomotors is powered by surface chemistry. They move by ejecting bubbles [8, 23, 24], or by a slip flow arising from chemical gradients (i.e., self-electrophoresis or self-diffusiophoresis) [25–27]. However, all chemically powered micro-/nanomotors require some kind of fuel in their environment, or on board, or both, which to say the least causes inconvenience. Alternatively, fuel-free micro-/nanomotors are gaining popularity in practical scenarios where the presence of chemicals or chemical reactions is not desirable [28, 29]. These micro-/nanomotors can be powered by an external magnetic field, by a DC or AC electric field, by light of various wavelengths and intensity, and by ultrasound.

Ultrasound, sound waves of a frequency beyond human hearing (>20 kHz), has long been used in manipulating microscopic or even nanoscopic objects [30]. More recently, the discovery of ultrasound-powered micro-/nanomotors opens a new chapter in its usefulness [31] and ushered in new possibilities of functional micro-machines in biologically relevant environments. In the remainder of this book chapter, we give an extensive review of the progress made in micro-/nanomotors powered by ultrasound, with an emphasis in their operating principles and their usefulness and limitations in biomedical applications.

This book chapter is organized as follows. In Sect. 2.2, we briefly review the fundamentals of ultrasound physics, in particular acoustic radiation forces and acoustic streaming, two concepts that are often encountered in the literature of micro-/nanomotors and critical in their designs. Ultrasound micro-/nanomotors of four types, namely, microrod streamers, bubble streamers, flagella streamers, and acoustic jets, are then thoroughly described and discussed in Sect. 2.3. Finally, in Sect. 2.4, we comment on the future prospects of ultrasound-powered micro-/nanomotors. Throughout this book chapter, we connect the underlying principles of ultrasound-related physical effects to the propulsion of a micro-/nanomotor, and

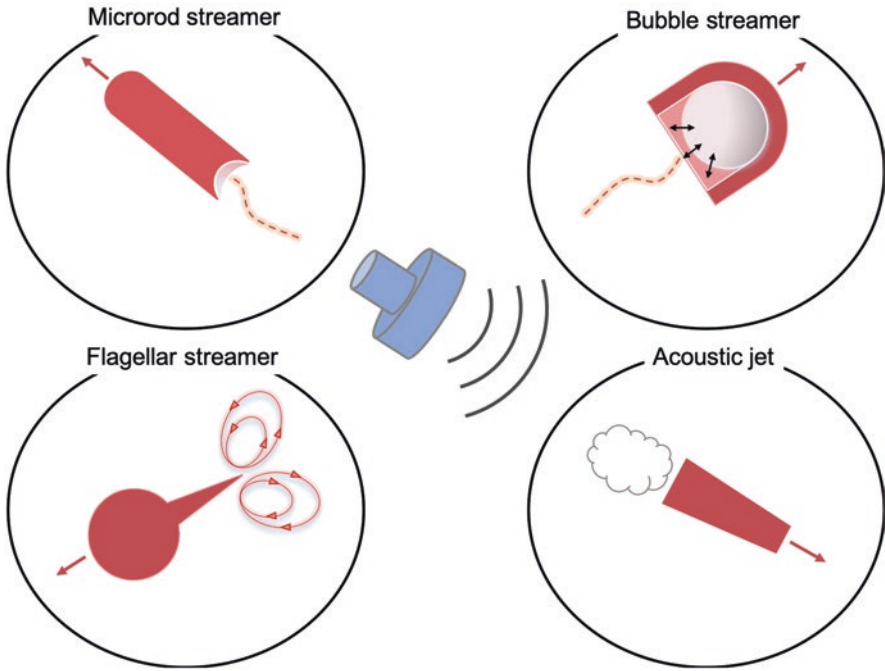





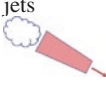
Fig. 2.1 A general scheme of the four types of ultrasound micro-/nanomotors discussed in this book chapter

highlight the various challenges that needed to be addressed before these micro-/nanomotors can be translated into clinical scenarios. It is our sincere hope that this book chapter will serve as an access point for scientists and engineers interested in the development of micro-/nanomachines (Fig. 2.1; Table 2.1).

2.2 Fundamentals of Ultrasound Physics

Before we discuss the various types of nanomotors powered by ultrasound, it is instrumental to give a brief introduction to how ultrasound affects a colloidal particle suspended in water. In particular, we focus on two acoustic effects—acoustic radiation forces and acoustic streaming—that are most relevant for micro-/nanomotors in ultrasound. Readers interested in the details of these effects are directed to more comprehensive reviews on acoustic radiation forces [30, 32] and acoustic streaming [33, 34] (Fig. 2.2).

Table 2.1 Four types of ultrasound-powered micro-/nanomotors

Motor type	Operating principles	Main features	Operating frequencies	Limitations
 <p>Microrod streamers</p>	Steady fluid streaming around an asymmetrically shaped colloidal particle	<ul style="list-style-type: none"> Operates on a levitational plane 3 modes of motion Most popular for biological applications 	<ul style="list-style-type: none"> Depends on the size of the acoustic chamber 3–4 MHz for a chamber of 200 μm tall 	<ul style="list-style-type: none"> Requires a standing wave Doesn't work for polymeric or symmetrically shaped particles
 <p>Bubble streamers</p>	Cavitation microstreaming near an oscillating, trapped microbubble	<ul style="list-style-type: none"> Only requires traveling waves Strong Bjerknes force leads to motor-motor and motor-structure attraction Able to manipulate colloidal particles, such as cells, and to move in 2D or 3D space Can be fabricated by lithography, 3D printing, or chemical/physical deposition + etching 	<ul style="list-style-type: none"> Related to the resonance frequency of the bubble, which is further governed by the bubble size MHz for bubbles of μm in sizes 	<ul style="list-style-type: none"> Fabrication can be complicated and resource-heavy, with limited yields Low reproducibility and short lifetime of the gas bubbles
 <p>Flagella streamers</p>	Microstreaming near a flexible body or a sharp edge	<ul style="list-style-type: none"> Only requires traveling waves The operating principle can also be used to manipulate microparticles 	<ul style="list-style-type: none"> Typically in the high kHz regime but difficult to predict 	<ul style="list-style-type: none"> Requires higher acoustic pressures than bubble streamers Difficult to predict the resonant frequency
 <p>Acoustic jets</p>	Droplet vaporization ignition: fast vaporization of liquid droplets trapped in a microtube via focused ultrasound	<ul style="list-style-type: none"> Powerful and easy to activate Only requires traveling waves 	<ul style="list-style-type: none"> Typically in the MHz regime 	<ul style="list-style-type: none"> Can only be activated once Poor control over speed or directionality

2.2.1 Acoustic Radiation Forces

An object in the path of a propagating sound wave generates its own scattered wave and in doing so experiences pressure because of momentum transfer. This pressure, termed acoustic radiation pressure, when integrated over the entire body of the object, leads to a net force termed acoustic radiation forces, whose presence has

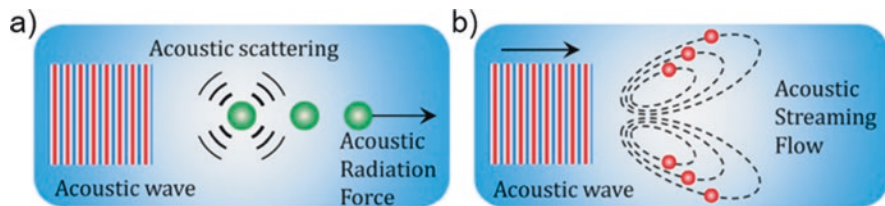


Fig. 2.2 Cartoon illustrations of acoustic radiation forces and acoustic streaming. **(a)** Acoustic wave is scattered by a large particle. The original and the scattered acoustic waves generate an acoustic radiation force on the particle. **(b)** Acoustic waves generate streaming in the fluid and small particles are convected by the streaming flow. The dynamic of a particle under ultrasound can be dominated by either the acoustic radiation force or acoustic streaming, depending on the diameter and density of the particle. Reproduced with permission [35]. **Copyright 2016, American Chemical Society**

long been known since the nineteenth century. Later, a series of seminal work from King, Yosioka and Kawasima, and Gorkov established the governing equations that describe the acoustic radiation forces acting on a small particle immersed in a viscous liquid [32]. For the special case of a standing ultrasound wave (e.g., typical for the microrod streamers discussed below), the acoustic radiation force becomes quite strong and is governed by [32]:

$$F = - \left(\frac{\pi p_0^2 V \beta_w}{2\lambda} \right) \Phi(\beta, \rho) \sin(2kd) \quad (2.1)$$

where k is the wave number, λ is the wavelength, V is the volume of the particle, and d is the distance between the particle and the node or antinode of the standing wave. The magnitude of this force is proportional to the square of the pressure amplitude (p_0) and the volume of the particle V . The term $\Phi(\beta, \rho)$ in Eq. 2.1 is the acoustic contrast factor, given by:

$$\Phi(\beta, \rho) = \frac{5\rho_c - 2\rho_w}{2\rho_c + \rho_w} - \frac{\beta_c}{\beta_w} \quad (2.2)$$

where ρ_c and ρ_w are the density of the particle and medium, respectively, and β_c and β_w are the compressibility of the particle and medium, respectively. If $\Phi(\beta, \rho) > 0$, the particle will be forced to the pressure nodes; otherwise, it will move to the antinodes. Intuitively, the larger the absolute value of $\Phi(\beta, \rho)$ of the particle, the larger the radiation force it experiences, and the stronger it responds to an incoming sound wave. This will become important in Sect. 2.3.1 for understanding why metal particles (of a larger ρ and β) are more efficient micro-/nanomotors in ultrasound than polymers.

Under the effect of an acoustic radiation force, a colloidal particle typically found in a micro-/nanomotor experiment, such as metal rods, polymer microspheres, etc., is transported to the pressure node of the standing wave, which often takes the

form of a nodal plane positioned vertical to the sound propagation direction in an acoustic chamber. The number and position of the nodal plane is governed by:

$$h = \frac{1}{2} n \lambda = \frac{1}{2} n \frac{c}{f}, n = 1, 2, 3, \dots \quad (2.3)$$

where h is the height of the acoustic chamber, λ is the wavelength of ultrasound, f is its frequency, n are integers, and c is the speed of sound in the medium ($c = 1492 \text{ m}\cdot\text{s}^{-1}$ in water). For a typical chamber of $200 \text{ }\mu\text{m}$ tall (e.g., made of two glass slides stacked on each side of a silicone spacer with a circular hole) and filled with water, the lowest resonance frequency is 3.73 MHz , corresponding to a nodal plane located at half the height of the chamber, $100 \text{ }\mu\text{m}$ from the floor or the ceiling. Doubling the frequency will generate two nodal planes that are evenly separated in the chamber by $66.7 \text{ }\mu\text{m}$ and so on. However, we note that experiments with ultrasound micro-/nanomotors have rarely explored a system with more than one nodal plane.

In a typical experiment, upon turning on an ultrasound wave of a resonance frequency, colloidal particles that have settled on the chamber bottom are quickly levitated to the nodal plane by an acoustic radiation force along the wave propagation direction. Once there, levitated particles experience an additional lateral acoustic radiation force that transports them to specific points on the nodal plane of maximum acoustic kinetic energy density, likely caused by an inhomogeneity from the energy distribution on the nodal plane for a number of possible reasons [30]. This lateral force is especially important in understanding the distribution of microrod streamers into rotating rings, and why they are only found at certain spots on the nodal plane (see Sect. 2.3.1).

What we have described above is known as the primary acoustic radiation force, levitating particles to a nodal plane and transporting them to certain “hot spots” on the plane. A secondary acoustic radiation force is also present between two colloidal particles, arising from the interaction between their scattered waves. This is also known as Bjerknes forces [36–38] and is attractive for particles on the same levitation plane but repulsive for those located along the wave propagation direction. The Bjerknes force is significant only when particles are located in close proximity, or if they are very compressible (e.g., bubbles or cells). It is partly responsible for the clumping of microrod streamers on a levitation plane (Sect. 2.3.1), and for the attraction between a bubble streamer to a nearby substrate (Sect. 2.3.2).

To summarize, ultrasound-powered micro-/nanomotors that we describe in this chapter experience a total of three types of acoustic radiation forces. An axial radiation force moves the particles strongly toward the pressure node (in the case of a standing wave), or weakly toward the pressure minimum in the case of traveling wave (often ignored in micro-/nanomotor literature). Once a particle is on a nodal plane, lateral radiation forces push it to acoustic hot spots defined by the energy landscape on that plane. Finally, secondary radiation forces (Bjerknes forces) induce the aggregation of nanomotors, or their attachment to the substrate in the case of bubble streamers. Note that none of the above forces directly propels a micro-/

nanomotor into autonomous motion. Rather, these motors are powered either by surface microstreaming (Sect. 2.3.1–2.3.3) or by jet streaming (Sect. 2.3.4), effects that we elaborate below.

2.2.2 Fundamentals of Acoustic Streaming

Acoustic streaming, also known as steady streaming, is a net fluid flow caused by the acoustic energy dissipation in a viscid fluid. When propagating in a fluid, acoustic waves force fluid elements to oscillate sinusoidally. The acoustic waves keep a constant shape during the propagation if it is an ideal fluid; therefore the time-average displacement of the fluid elements is zero. However, a viscous fluid will introduce fluctuations to the velocity and amplitude of the oscillation, resulting in a non-zero time-average displacement of the fluid elements, i.e. a net fluid flow. This nonlinear phenomenon was first theoretically studied by Rayleigh via a successive approximation technique [39], in which the acoustic streaming was given by the higher orders governing equations. The later development of the acoustic streaming theory has followed Rayleigh approach. However, it is difficult to have a unified analytical description for all the situations since acoustic streaming can vary dramatically in its speed, length scale, flow patterns, and so on. Numerical simulation has been extensively applied to study streaming that occurs in various circumstances. Here we will qualitatively introduce two common types of acoustic streaming. More detailed theoretical discussions are beyond the scope of this chapter, but interested readers may refer to the reference [33, 34, 40].

Depending on the mechanism of the acoustic energy dissipation, acoustic streaming could be classified as being driven by either bulk dissipation or boundary dissipation. The acoustic streaming driven by bulk dissipation is called as “Eckart streaming” or “quartz wind.” When an acoustic wave propagates in a bulk fluid, the viscosity of the fluid causes the amplitude of the acoustic pressure to decrease along the direction of the propagation. The dissipated energy converts to a steady momentum flux, forming a jet of fluid moving in the same direction. Since the acoustic attenuation in fluid is typically small and is proportional to the square of the acoustic frequency, significant Eckart steaming can only be observed in cases of high acoustic frequency and amplitude. It also usually requires the dimension of the fluid container in the propagating direction to be much larger than the wavelength of the acoustic wave. This type of acoustic streaming is less relevant to the propulsion of micro-/nanomotors, unless it induces bulk convection and leads to motor drifting.

The streaming driven by boundary dissipation is generally introduced at a solid/fluid interface. As the solid boundary is no-slip, the velocity of the acoustically oscillated fluid elements decreases dramatically to zero at the boundary from a non-zero velocity away from the boundary. The velocity drop is confined in a thin viscous boundary layer, the *Stokes layer*, with a thickness of $\delta = \sqrt{2\nu/\omega}$. Here ν is the kinematic viscosity of the fluid, and ω is the angular frequency of the acoustic wave, and δ is in submicron scale for megahertz acoustic waves propagating in water. The

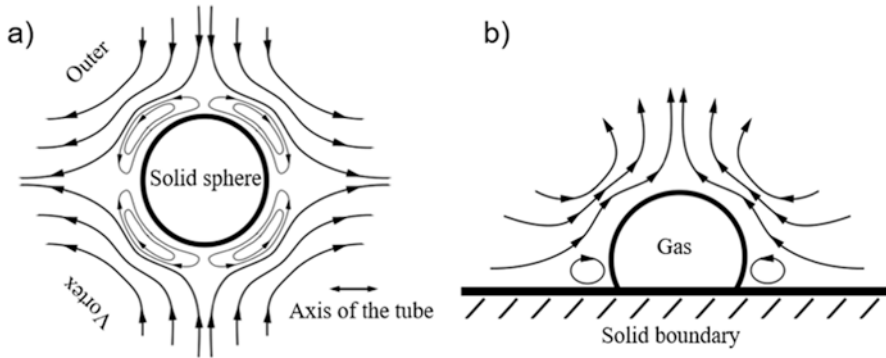


Fig. 2.3 Acoustic streaming. (a) Inner and outer layer acoustic streaming patterns around a rigid sphere in a standing acoustic field in a Kundt's tube, (b) acoustic cavitation microstreaming pattern generated by a gas bubble resting on a solid boundary. Reproduced with permission [43]. Copyright 2005, Acoustical Society of America

significant energy dissipation in such a thin layer leads to strong vortices inside this layer, named as inner boundary layer streaming or “Schlichting streaming.” Because of fluid continuity, the inner boundary layer streaming further generates counter-rotating streaming in the bulk of the fluid, called the outer boundary layer streaming or “Rayleigh streaming.” Inner and outer boundary layer streaming are typically observed in microfluidic chambers or channels with a characteristic length scale close to or smaller than the acoustic wavelength. The streaming pattern introduced by standing acoustic waves in rectangular-shaped channels or on the surface of spherical particles has been extensively analyzed and well understood both theoretically and experimentally [41, 42]. Figure 2.3a indicates a typical boundary-driven streaming pattern around a rigid sphere in a standing acoustic field. The inner and outer layer vortices are symmetrically distributed around the sphere, leading to zero net hydrodynamic force on the sphere [43].

Fluid/fluid or gas/fluid interfaces, such as those found near an oscillating bubble for certain types of motors described below, can also cause energy dissipation and acoustic streaming due to the mismatch of their viscosities. For fluids with high viscosity, the acoustic streaming pattern is similar to that on a solid/fluid interface, which includes the inner and outer boundary layer streaming. When the viscosity decreases to a certain value, the inner boundary layer disappears, leading to reversed outer boundary layer streaming. Mathematically, the streaming generated by a low viscosity fluid or gas boundary is much weaker than that generated by a solid boundary. However, gas bubbles submerged in fluid could be forced to oscillate volumetrically by acoustic waves, and the oscillation of the interface will significantly enhance the streaming. The acoustic streaming generated by oscillating gas bubbles is called *cavitation microstreaming*. At the resonant frequency, a gas bubble oscillates with the highest amplitude, leading to the strongest cavitation microstreaming that could be several orders of magnitude stronger than that induced by a solid particle of a similar size. For a bubble that is resting on a solid boundary, the

asymmetrical boundary condition leads to directional cavitation microstreaming (Fig. 2.3b) and a net hydrodynamic force on the bubble. This net force is ultimately responsible for the propulsion of a bubble streamer, discussed in Sect. 2.3.2.

Acoustic streaming of various unique properties has been implemented to different applications. For example, Rayleigh streaming was utilized to balance the gravitational force and achieve precise position control of microparticles in the vertical direction [44], while cavitation microstreaming has been widely applied for efficient fluid mixing and pumping in microfluidic devices due to its high speed [45]. In the following sections, we will see how acoustic streaming contributes to the active propulsion of micro-/nanomotors.

2.3 Designing Ultrasound Micro-/Nanomotors

In this section, we will introduce four specific types of micro-/nanomotors powered by ultrasound. The first three, microrod streamers, bubble streamers, and flagella streamers, all rely on some sort of surface microstreaming to swim. The last type, acoustic jets, is somewhat unusual and takes advantage of the sudden expansion in volume of an organic droplet trapped in a tube. In each case, we detail the notable studies reported in the literature, explain the fundamental operating mechanism, and comment on its usefulness/limitation in biomedical applications.

2.3.1 *Microrod Streamers*

This type of ultrasound micromotor refers to metallic microrods that autonomously translate, rotate, and spin in MHz ultrasonic standing waves, at a speed of ~ 100 body lengths $\cdot s^{-1}$. They are arguably the most studied type of ultrasound-powered micro-/nanomotors and have received the most attention in the form of preliminary reports of biomedical applications.

Early Discoveries

A collaborative effort between the labs of Mauricio Hoyos at ESPCI in France and that of Thomas Mallouk at Penn State in the USA discovered in 2011 that gold microrods of a few μm long and 200–300 nm in diameter [31], synthesized by electroplating in porous templates, were able to move at a dazzling speed of $\sim 200 \mu m \cdot s^{-1}$ (~ 100 body lengths $\cdot s^{-1}$) when levitated in a cylindrical half-wavelength acoustic chamber vibrating at a frequency of ~ 3.7 MHz. They did so on a levitation plane (i.e., nodal plane) halfway between the top and bottom surface of the chamber. This came as a surprise because the gold rods were orders of magnitude smaller than the sound wavelength of $\sim 400 \mu m$ irradiating on them. Beyond directional motion,

other striking observations were made, including the spontaneous assembly into a large ring of spinning rods loosely connected to each other, and gold rods that furiously and independently rotated in plane. These different modes of motion were often concurrent but sensitive to the locations on the nodal plane and the ultrasound frequency. The publication detailing these observations in 2012 [31], of which Wei Wang was an author, has been cited over 300 times and has led to many subsequent studies on mechanisms, on biomedical applications, and on basic sciences. These will be described in detail below.

Mechanisms

The discovery of surprising propulsion for micro-/nanomotors often means an initial confusion on its mechanism. This was the case during the early years following the discovery of bimetallic microrods moving by self-electrophoresis [7, 47, 48], and certainly the case for metallic microrods moving in ultrasound. In the original paper reporting this discovery [31], the authors eliminated the possibility of rods moving by ultrasonically enabled chemistry, and instead proposed that it was rather an asymmetric scattering of sound waves on a rod of asymmetric shape. In particular, the authors noted, upon close examination of the rod morphology under SEM (see Fig. 2.4b), that the electrochemically synthesized microrods were often concave on one end and convex on the other, resembling a tiny rocket ship. This non-uniformity in shape was likely due to how the plating solutions wet the alumina membrane. Following this observation, the authors argued that sound waves would be concentrated at the concave end but scattered at the convex end, creating an acoustic pressure gradient along the rod and propelling it by a mechanism termed “self-acoustophoresis.” Note that this word is derived from acoustophoresis, i.e., the transport of particles in a gradient of acoustic radiation forces [49].

However, as mentioned above, the mismatch between the dimension of microrods and that of the incoming sound waves strongly suggests that this self-acoustophoresis, if exists, would be very minor. On the other hand, the shape

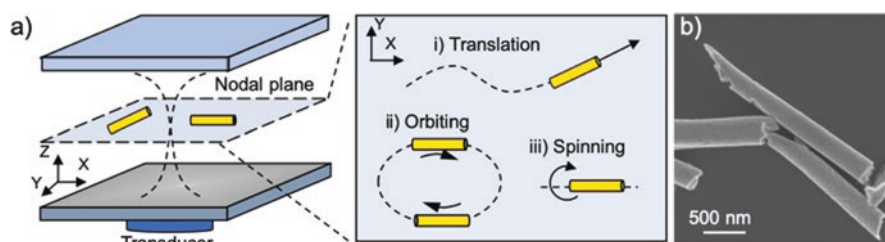


Fig. 2.4 Microrod streamers: operation. (a) Three types of behaviors (directional motion, orbiting, and spinning) observed with metallic microrods levitated by standing ultrasonic waves; (b) a scanning electron micrograph of a metallic microrod fabricated by electrodeposition, showing the sharp edges and uneven features on the rods. Reproduced with permission [46]. **Copyright 2017**, American Chemical Society

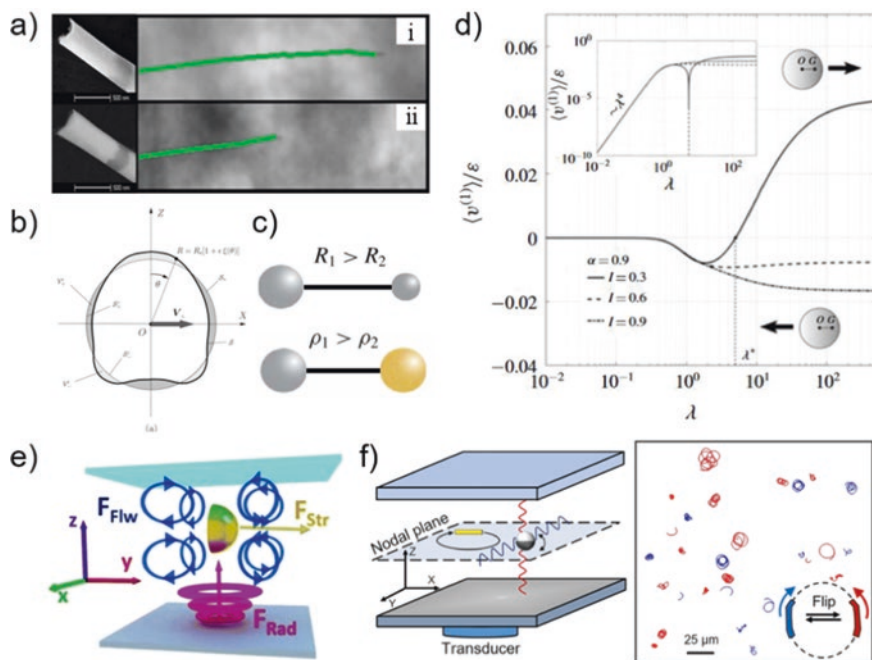


Fig. 2.5 Propulsion mechanisms of microrod streamers. (a) Metallic nanorods with a more concave end (i) swim faster than one with flat end (ii) in ultrasound. Reproduced with permission [50]. Copyright 2013, American Chemical Society. (b) Geometry of an asymmetrically shaped sphere studied for its propulsion in ultrasound. Reproduced with permission [52]. Copyright 2014, American Institute of Physics. (c) Dumbbell-shaped particles of two lobes of different sizes (top) or density (bottom) are studied for their acoustic propulsion. Reproduced with permission [53]. Copyright 2017, Cambridge University Press. (d) The direction of a bottom-heavy sphere propelled in ultrasound can be reversed when the frequency is larger than a threshold value. Reproduced with permission [54]. Copyright 2020, Cambridge University Press. (e) Acoustic propulsion of a metallic nanoshell via asymmetric surface streaming. Reproduced with permission [55]. Copyright 2016, Royal Society of Chemistry. (f) Metallic microrods and Janus microspheres twist and turn under ultrasound. Reproduced with permission [46]. Copyright 2017, American Chemical Society

asymmetry on a microrod seems to be necessary for effective propulsion, and an experiment by Garcia-Gradilla et al. showed that a microrod with a more profound concave end moved faster than one with a flat end (Fig. 2.5a) [50]. Moreover, it was noted in the original report that polymer microrods of similar shapes and sizes were not able to propel in ultrasound, but gold microspheres of a rough surface could [31]. Furthermore, a systematic study by Ahmed et al. [51] in 2016 shows that metal microrods preferred to move with the concave end forward, that a dense rod moves slower than a light rod, and that a rod made of two metals of different densities moves with the light end forward. These observations suggest a complicated interplay among ultrasound, surface morphology, and materials, which is further

connected to the acoustic properties of the particle. But how these properties give rise to propulsion remained mysterious in the early years.

An exciting breakthrough in understanding came in 2014 by Nadal and Lauga [52]. Inspired by the experimental observations of a metallic rod moving in ultrasound, but working independently from those experimental groups, Nadal and Lauga developed a model that qualitatively explained how the oscillation of an asymmetrically shaped near-spherical particle in ultrasound produces a net flow that moves it forward (Fig. 2.5b). Specifically, their mechanism centers around the concept of “asymmetric steady fluid streaming,” which essentially states that a nonzero net flow is produced by integrating the surface flow of an asymmetric particle oscillating with a finite Reynolds number. The propulsive speed of a micromotor is then directly proportional to the Reynolds number and its shape parameter, as well as the magnitude of its oscillation, which is further related to the parameters of the applied ultrasound and the acoustic properties of the particle. By inserting realistic values into this model, a speed of $\sim 20 \mu\text{m}\cdot\text{s}^{-1}$ was calculated for a microrod moving in ultrasound, one order of magnitude smaller than their actual speeds. Nevertheless, this theoretical study represents a giant leap in our understanding of how micro-/nanomotors move ultrasound.

A few years later, Collis et al. developed a modified theoretical framework (Fig. 2.5c), based on the same surface streaming effect, to explain how ultrasound powers micro-/nanomotors [53], with a focus on the previously reported dependence on the density distributions on the particle (i.e., the experimental work from Ahmed, ref. [51]). Compared with the model from Nadal and Lauga that assumed “a nearly spherical and homogeneous density particle in a low acoustic Reynolds number flow,” this new model by Collis et al. “is applicable to arbitrarily shaped axisymmetric solids with arbitrary density distributions that are being driven at arbitrary finite frequency.” To do so, this new model first studied a dumbbell made of two spheres of different sizes or densities (Fig. 2.5c), essentially working as two engines in tandem that cooperatively provide propulsion. Not only does the model agree with experiments that a rod with higher structural asymmetry moves faster, and that a rod moves with its lighter end forward, the most surprising and inspiring finding is that the directionality of a micromotor can reverse as the frequency is increased beyond a threshold, a prediction that is yet to be experimentally verified. Lauga and Michelin recently followed up on this work and provided an analytical description of the speeds of a sphere of inhomogeneous density under ultrasound [54]. Similar reversal in direction was found for varied frequencies (Fig. 2.5d).

Following the same surface microstreaming principle, a very recent theoretical paper by Voß and Wittkowski examined the propulsion of microparticles in traveling ultrasound waves instead of standing waves [56], a more realistic condition for real-life applications because standing waves are much more difficult to obtain and maintain. This theoretical work is in particular inspired by experiments by Soto et al. (Fig. 2.5e) [55], who demonstrated that metallic microcaps (“nanoshells”) move in standing wave ultrasound with the convex end leading, an observation in contrast to that reported by Ahmed et al. in which metallic microrods moved in ultrasound with their concave ends leading [51]. Specifically, Voß and Wittkowski

numerically solved the flow fields around asymmetrically shaped particles that are either half balls or cones, and either hollow inside or not. The major findings from their simulations are as follows: (1) a cup-shaped particle moves with its convex end leading, consistent with the report from Soto et al.; (2) pointed particles move faster than those with a rounded tip, and whether the particle contains a cavity is not important; and (3) the near-field flows around these particles are pusher-type. These results are inspirational for future designs of acoustic micro-/nanomotors of various shapes.

Beyond operating as micro-/nanomotors that move ballistically along a particular direction, microparticles in ultrasound are also able to rotate. They then become microrotors, a critical component in micromachinery that is potentially useful in minimally invasive surgery and micro-assembly. The rotating modes of motion were first identified in the original discovery of ultrasound micro-/nanomotors [31], where the authors noted strong in-plane rotation of metallic microrods (Fig. 2.4a ii) and spinning along their long axes (Fig. 2.4a iii). A later study by Balk et al. further quantified a surprisingly high spinning rate of 2.5 kHz [57]. As a result, tracer microspheres are seen to be advected by vortices around a spinning metallic micro-rod in ultrasound. A few years later, Sabrina et al. showed that gold microplates of twisted star shapes spontaneously rotated in ultrasound and their rotational direction was dictated by their structures [58].

Despite these experimental progress, mechanistic understanding of how microparticles rotate or spin in ultrasound has been still quite limited until recently, when Zhou et al. offered fresh insights on how ultrasound induces rotation (Fig. 2.5f) [46]. More specifically, they combined experimental results with acoustic theories to show that in-plane rotation for metallic microrods occurs predominantly at the resonance frequency and is due to the slightly bent shape of the electrochemically synthesized microrods. As the driving frequency is shifted slightly away from the resonance frequency, rotation gives way to directional motion. The axial spinning, on the other hand, is not related to shape asymmetry on the rod, but rather to the propagation of two sets of sound waves orthogonal to each other within the chamber. This theory states that a phase mismatch between these two waves creates a viscous torque that rotates a microparticle, trapped at the nodal plane where the two waves meet, at a spin rate that matches that observed in experiment.

To summarize, a collective effort from the experimentalists and theorists around the globe has put the various pieces of puzzles together and offer a consistent framework for understanding how ultrasound powers microparticles. On the experimental side, we now have a deeper appreciation of how the shape (in particular its asymmetry) and acoustic properties of a microparticle, as well as the power and frequency of the ultrasound, dictate the behavior of a micromotor in ultrasound. On the theoretical side, the local acoustic streaming around an asymmetrically shaped microparticle has been widely accepted as the dominant mechanism for its propulsion and in-plane rotation. Although some questions remain to be answered, such as the intricate coupling between the local streaming and the strong vortices around a spinning rod, the steady progress we have made over the years in understanding ultrasonic propulsion is truly remarkable and is ultimately

the key element in enabling the wide range of biomedical applications that we discuss below.

Biomedical Applications

Biocompatible, ultrasound-powered microrod streamers hold great promise for their use in practical biomedical applications. For example, micro-/nanomotors could deliver therapeutic payloads directly into a targeted region. Nevertheless, there is a need to develop novel methods to guide and steer them toward the target of interest. In this direction, ultrasound-powered microrod streamers have been coupled with magnetic segments composed of ferromagnetic materials that respond to externally induced magnetic fields for achieving directional guidance over pre-programmed paths. The external magnetic fields align a nickel magnetic segment embedded in a nanowire by applying a magnetic torque, thus redirecting the direction of locomotion in alignment with the magnetic field lines. Directional movement is possible by changing the orientation of the applied magnetic field. The nanowire can then be directed over complex trajectories and at all angles [59]. These ultrasound-powered nanorods have shown efficient locomotion control and guidance in diverse biofluids, including serum, saliva, and blood. More recently, nanorods coated with magnetite nanoparticles (Fe_3O_4) via electrostatic interactions reported long-lasting operation in high acidity environments under extended exposure, illustrating their potential use for gastrointestinal applications [60].

Ultrasound-powered nanorods have been used for triggered therapeutic release. Different pharmaceuticals have been loaded into the surface of nanorods using electrostatic interactions. Nanorods containing a negatively charged polymeric polypyrrole-polystyrene segment were loaded with positively charged brilliant green as a model drug. The polymeric segments protonate in the presence of acidic environments, causing the responsive release of the loaded drug (Fig. 2.6a) [50]. In another case, porous nanorods coated with an anionic coating were loaded with doxorubicin. The high surface area of the nanorod increased its drug loading capacity and induced a photothermal effect when exposed to NIR, resulting in the triggered release of the loaded doxorubicin [9].

Ultrasound-propelled nanorods have also been used for detoxification applications, where active biological coatings provide pathogen and toxin remediation functionalities. For example, nanorods functionalized with concanavalin A, a protein that binds with bacteria membrane polysaccharides, were used for “on-the-fly” capture and isolation of *Escherichia coli* bacteria [50]. Porous nanorods covalently functionalized with lysozyme, an enzyme capable of cleaving bacteria walls, were used for killing Gram-positive *Micrococcus lysodeikticus* and Gram-negative *Escherichia coli* bacteria [61]. The rapid motion of the nanorods induced fluid mixing and increased the interaction between the functionalized lysozyme and the pathogen, resulting in a dramatic improvement in the antibacterial efficiency over unpowered nanorods. Using a similar principle, asparaginase-functionalized nanorods were used for inhibiting cancer cell growth [62].

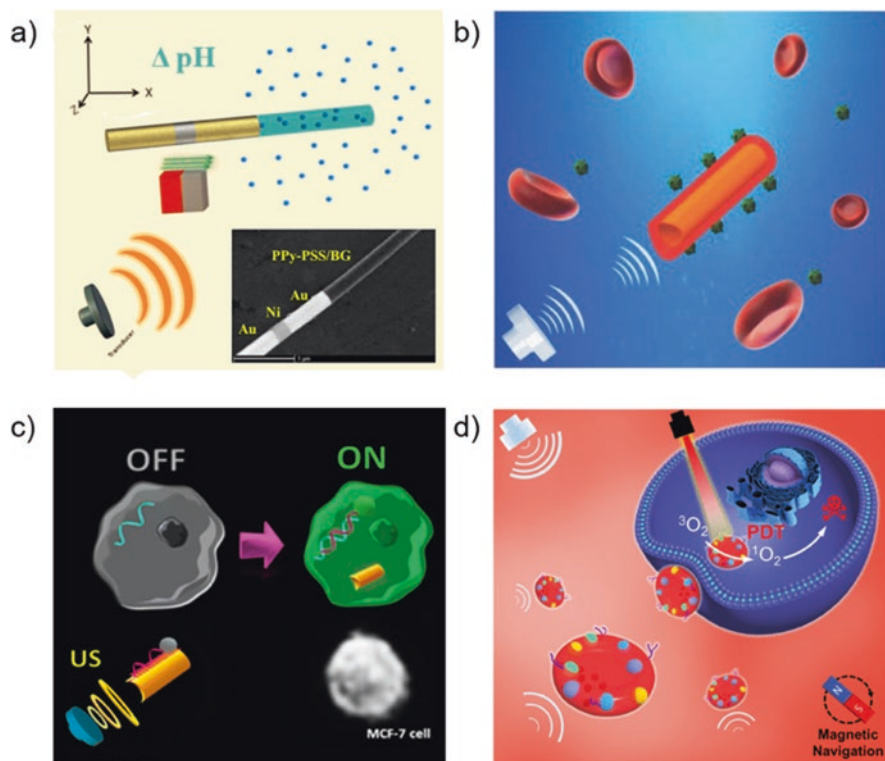


Fig. 2.6 Use of ultrasound-powered nanomotors for biomedical applications. (a) Use of nanorods for pH-triggered drug release. Reproduced with permission [50]. Copyright 2018, American Chemical Society. (b) Use of nanorods coated with red blood cell membrane for toxin absorption. Reproduced with permission [63]. Copyright 2015, Wiley-Blackwell. (c) Use of nanorods as intracellular mRNA fluorescent sensor. Reproduced with permission [66]. Copyright 2015, American Chemical Society. (d) Use of ultrasound-propelled red blood cells for photothermal therapy. Reproduced with permission [72]. Copyright 2019, American Chemical Society

Cell membrane-coated nanorods have been used for isolating pathogens and toxins. Nanorods coated with red blood cell can absorb melittin (a pore-forming toxin) using their external red blood cell coating as a sponge. This design enabled efficient locomotion in whole blood and demonstrated the reduction of hemolysis in red blood cells exposed to these toxins (Fig. 2.6b) [63]. An extension of this work combined red blood cells and platelets into a single surface coating to mimic the biological functions of these plasma cells. The platelet membrane served to capture and isolate *Staphylococcus aureus* bacteria, while the red blood cell membrane was used to absorb the secretions of α -toxin by the adhered bacteria [64].

Ultrasound-powered nanorods can also be internalized and move inside living HeLa cells after incubation with the cells for periods longer than 24 h [65]. This development has led to different intracellular applications, including cargo delivery and sensing. For example, ultrasound-powered nanorods were used to detect

miRNA from cancer cells. The nanorods were coated with graphene oxide layers that bond via electrostatic interactions with fluorescently tagged single-stranded DNA. Initially, the fluorescent tag was quenched by its interaction with the graphene oxide. Once the nanorod is internalized by a cancer cell, preferential hybridization of the probe with target miRNA dislodges it from the surface of the nanorods, resulting in the recovery of fluorescence (Fig. 2.6c) [66]. This off-on strategy was also reported for detecting RNA in human papillomavirus-positive cells [67]. The use of ultrasound-powered nanorods has also been explored for gene silencing via siRNA [68] and Cas9 [69]. In both cases, the authors reported the knockout of GFP expression by the target cells. On the other hand, ultrasound-propelled nanorods have also been used for the delivery of therapeutic cargos including oxygen [70], caspase-3 for cell apoptosis [71], and photodynamic cancer therapeutic agents (Fig. 2.6d) [72, 73].

Practical Considerations

Although diverse biomedical proof of concept applications has been proposed using ultrasound-propelled nanorods, we need to consider their clinical translation outlook.

- (a) The first challenge lies in generating acoustic standing waves inside the human body. The levitation plane where the nanorobots operate has been generated in relatively small acoustic resonators in lab-on-a-chip devices. Thus, before any acoustic nanomotor design is tested in any animal models, there is a requirement of generating controllable and tunable acoustic standing waves inside the body. Moreover, the presence of standing waves could result in an aggregation of plasma cells, forming undesired thrombolysis.
- (b) In case these limitations are resolved, we need to consider the material composition of nanorods. Most designs are composed of gold that, although is a biocompatible material, is also bio-accumulable. As a result, the use of ultrasound-propelled nanorods would require retrieval strategies. The use of metals such as zinc or iron that dissolve over time could be a solution, but metals with lower density than gold have shown less efficient locomotion [51]. Moreover, the surface coating could help avoid immune response and biofouling by the accumulation of proteins and biological agents.
- (c) Another potential use for nanorods is their usefulness in sensing on a lab-on-a-chip device. As discussed in the biomedical application section, the use of ultrasound-powered nanorods can preconcentrate biological targets on the levitation plane and enhance the contact of active materials with their target. As a result, they could be used for environmental remediation and intracellular sensing applications. Nevertheless, the reported nanorods have limited spatiotemporal motion resolution inside living cells.

- (d) Finally, current ultrasound resonators require specialized equipment and techniques, while portable models could expand the use of these microrod streamers outside of specialized places such as hospitals or research labs.

Usefulness in Basic Sciences

Beyond showing promise in various biomedical applications that we discussed above, ultrasound-powered microrod streamers are also useful in the study of basic sciences, in particular in dynamic self-assembly and in the studies of active colloids. We offer a brief introduction in this section, whereas an expanded discussion can be found in a review article published earlier [74].

On the topic of dynamic assembly, Ahmed et al. have studied how ultrasonically powered metallic microrod motors, which have a magnetic segment embedded in them, would spontaneously assemble and disassemble (Fig. 2.7c) [75]. Interestingly, dimers, trimers, and multimers formed as the ultrasound forces that drive them apart compete with the magnetic dipolar attraction. The distribution of each type of

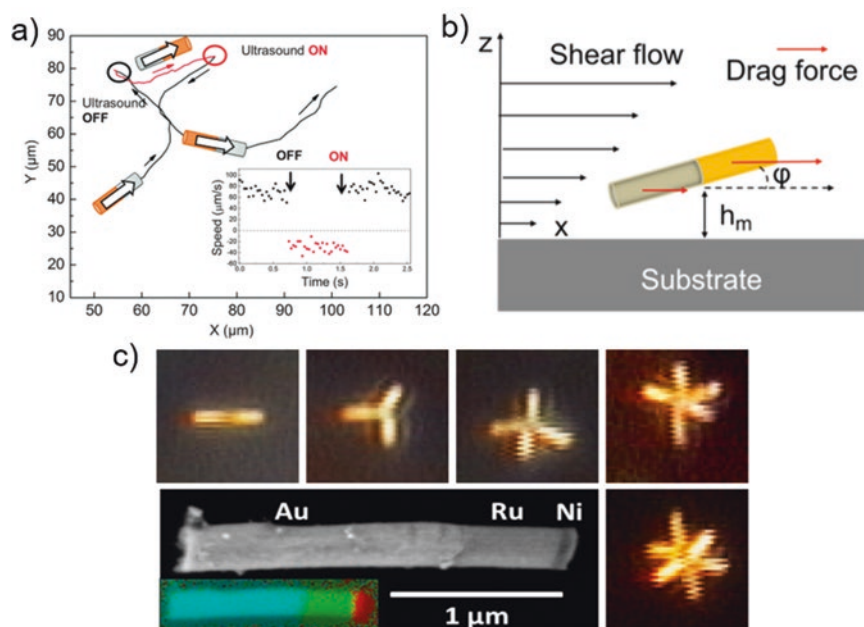


Fig. 2.7 Microrod streamers: usefulness in basic sciences. (a) Trajectory and speed changes (inset) of a levitated bimetallic micromotor as the ultrasound power is switched on and off. Reproduced with permission [76]. Copyright 2015, Royal Society of Chemistry. (b) Schematic illustration of how a metallic rod orientates in a flow. Reproduced with permission [78]. Copyright 2017, American Chemical Society. (c) Segmented bimetallic gold-ruthenium nanorods with a thin Ni segment assemble into few-particle, geometrically regular dimers, trimers, and higher multimers in ultrasound. Reproduced with permission [75]. Copyright 2014, American Chemical Society

cluster can then be controlled by varying the ultrasound power (but not the strength of the magnetic interaction that was fixed), enabling the identification of the binding energies of the individual rods within a cluster in a way inspired by chemical kinetics. A second study by Wang et al. examined how a group of nanomotors propelled by both ultrasound and chemistry assemble and disassemble in the combined forces (Fig. 2.7a) [76]. The interesting observation of active micro-/nanomotors escaping from an acoustic trap is further discussed in a separate study by Takatori et al. [77].

On the topic of active colloids, the upstream or downstream movement (i.e., positive or negative rheotaxis) of ultrasound-powered microrod streamers was studied in shear flows (Fig. 2.7b) [78]. When H_2O_2 was also present, the bimetallic microrods were dually propelled. By controlling the magnitude and directionality of the ultrasonic propulsion, both positive and negative rheotaxis can then be realized.

2.3.2 Bubble Streamers

Mechanism

Acoustic waves can generate, oscillate, and destroy gas bubbles in a fluid, and all the phenomena could be utilized to develop micro-/nanomotors [79, 80]. In this section, we will focus on the acoustic bubble streamers that are propelled by continuous cavitation microstreaming (described in Sect. 2.2.2). The common design of the bubble streamers comprises one or more microscale cavities with orifices (see examples in Fig. 2.8). The cavities are typically fabricated from or coated with hydrophobic materials, so that gas bubbles can be trapped in the cavities as they are immersed in a fluid. The gas/fluid interfaces are located at those orifices. Upon exposure to the acoustic waves, a bubble starts to oscillate and generates directional cavitation microstreaming at the orifice. Consequently, the microstreaming exerts forces on the microcavities in the opposite direction of the streaming and propels it forward. The acoustic waves are usually generated by an acoustic transducer that is attached to the fluidic container or immersed in the fluid.

The velocity of the cavitation microstreaming is determined by the amplitude of the bubble's oscillation. A bubble has a maximal amplitude of oscillation when the acoustic wave frequency matches its resonant frequency. For a spherical gas bubble that is free of any boundary restrictions, and neglecting surface tension and viscous attenuation, the acoustic resonant frequency is given by the Minnaert resonance [81]:

$$f = \frac{1}{2\pi a} \sqrt{\left(\frac{3\gamma p_A}{\rho}\right)} \quad (2.4)$$

where a is the radius of the bubble, $\gamma-1.4$ is the adiabatic coefficient, p_A is the ambient pressure, and ρ is the density of the fluid. When the gas bubble is trapped in a cavity, the resonant frequency could shift, depending on the size and shape of the cavity. However, this shift is usually small, and the new resonant frequency could be

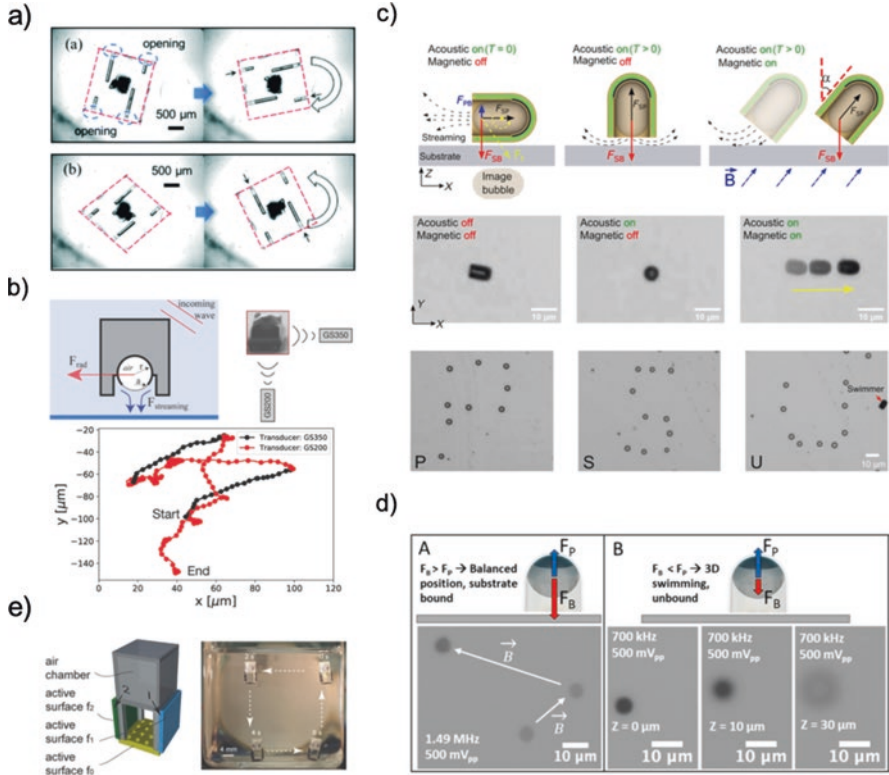


Fig. 2.8 Bubble streamers. (a) A bubble streamer that includes two different bubble sizes was rotated by selectively exciting the bubbles with different acoustic frequencies. Reproduced with permission [85]. Copyright 2016, Royal Society of Chemistry. (b) A 3D printed bubble streamer that could hover on the substrate and be guided by the direction of the traveling acoustic waves. Reproduced with permission [86]. Copyright 2018, Wiley-VCH. (c) A high bubble-to-streamer volume ratio streamer demonstrated a self-alignment behavior and required an external magnetic field to initial its translation. Multiple 4 μm silica particles were arranged into letters “PSU” on the substrate by such a swimmer. Reproduced with permission [87]. (d) A microbubble streamer switched from 2D motion to 3D motion when the acoustic wave changed from a bubble’s resonant frequency to a shape resonant frequency. Reproduced with permission [88]. Copyright 2020, American Chemical Society. (e) Schematic of a macroscale bubble streamer made from functional bubble surfaces. Each surface has its own resonant frequency. 3D motion was demonstrated by selectively activating the surfaces. Reproduced with permission [89]. Copyright 2017, Wiley-VCH

experimentally determined by scanning the driving frequency around the Minnaert resonant frequency of a spherical bubble with the equivalent volume. Theoretical prediction of the resonant frequency of the bubble streamers has also been studied by a few groups. Oguz et al. described the resonant frequency of a gas bubble that

is partially filled, i.e., an one-end-open tube, as $f = \frac{1}{2\pi} \sqrt{\left(\frac{kP_A}{\rho L_0 L_B}\right)}$, where L_B is the

length of the bubble and L_0 is the length of the liquid column between the bubble interface and the exit of the tube. k is a frequency-dependent parameter and satisfies

$1 \leq k \leq \gamma$ [82]. Ren et al. further considered the surface tension and provided a correction factor to Oguz's equation,

$f_c = f \cdot \left(1 + \frac{4\tau L_B}{kP_A a^2} \right)$, where τ is the surface tension of the liquid-gas interface [83]. However, the surface tension term is comparatively small if L_B and a are of the same order of magnitude. For a spherical

shape streamer, Bertin et al. predicted a frequency that scales as $f_{th} \sim \left(\frac{n^3 \tau}{\rho a^3 \theta_0^3} \right)^{1/2}$,

where $\theta_0 = \sin^{-1}(l/a)$ is the azimuthal angle of the orifice, l is the aperture size of the orifice, and n is the shape mode number [82]. It is worth noting that a gas bubble could have multiple resonant frequencies because of the presence of multiple oscillation modes. Finally, at the resonant frequency, the propulsion force F generated by the microstreaming is proportional to the square of the amplitude of the oscillation, which is further proportional to the input voltage from the acoustic transducers V_{pp} . Therefore, $F \sim V_{pp}^2$.

Notable Studies

The first bubble streamer was demonstrated by Dijkink et al. in 2006 [84]. This pioneering bubble streamer was made from a commercial Teflon tube that has one end sealed with glue. The 2–4-mm-long streamer has a 750 μm outer diameter and 250 μm inner diameter, and the resonant frequency was around 1.5 kHz. A maximum speed of 10 $\text{mm}\cdot\text{s}^{-1}$ (~ 3 body lengths $\cdot\text{s}^{-1}$) was observed. Despite the simple design and the preliminary results, they provided both experimental and theoretical strategies for studying the resonant frequency of a trapped bubble, the streaming pattern of such a design, and the propulsion force generated by the streaming. They also pointed out the direction to achieve diverse motions by integrating multiple bubbles oscillating at different frequencies.

From the perspective of applications in microfluidics and cell-level biomedical research, swimmers that are in the micrometer scale are preferred. Feng et al. later introduced a photolithography process for fabricating bubble streamers [90]. This method allowed them to precisely control the size and location of the gas tubes in the streamer. They were able to shrink the diameter of the gas tube into 60 μm , even though the length of the tube and the longest scale of the streamer are still a few hundreds to thousands of micrometers. In this case, the streamers were propelled by acoustic waves above 10 kHz and input voltages of over 100 V_{pp} and moved at 45 $\text{mm}\cdot\text{s}^{-1}$ (~ 50 body lengths $\cdot\text{s}^{-1}$). By combining multiple gas tubes with different lengths in one streamer and by arranging them in different orientations, they demonstrated 2D steerable and rotational motions (Fig. 2.8a) [85]. Similarly, Ahmed et al. developed a photopolymerization-based method to fabricate micro-size bubble streamers [91]. With a simple microscope, they could fabricate streamers smaller than 250 μm and place multiple gas tubes with different diameters in the streamer.

The diameters of the gas tubes are less than 100 μm , corresponding to resonant frequencies ranging from 40 kHz to 100 kHz. The streamers achieved a maximum speed of 8 $\text{mm}\cdot\text{s}^{-1}$ (50 body lengths $\cdot\text{s}^{-1}$) at an input voltage of 7 V_{pp} . Swimming in viscous fluids such as glycerol and hydrogels was also demonstrated.

In order to stabilize the gas bubbles and improve the usefulness of the bubble streamers in practical applications, Bertin et al. applied a high-resolution 3D laser printing method to reduce the size of streamer and the orifice [86]. The diameter of the spherical bubbles is 10–20 μm and the orifice of the streamers is around 5 μm . The streamers responded to ~ 320 kHz acoustic waves and moved for a few hours in salted water. Using 3D laser printing for fabrication significantly improved the versatility of the bubble streamers. Louf et al. printed swimmers (~ 20 μm) that had the bubble/water interface pointed toward the substrate (Fig. 2.8b) [86]. Such an orientation allowed the swimmers to hover above the substrate and move with low friction. A maximum speed of 350 $\text{mm}\cdot\text{s}^{-1}$ (17,500 body lengths $\cdot\text{s}^{-1}$) was demonstrated. They claimed that the bubble streamer was lifted by microstreaming and translate by acoustic radiation forces. The direction of the swimmer could be controlled by the direction of the acoustic waves.

Ren et al. further reduced the size of the streamers to less than 8 μm (2–4 μm gas bubble diameter) with the same 3D printing technique [83]. The high gas bubble to streamer volume ratio resulted in a secondary Bjerknes force that is comparable to the microstreaming propulsion force between the substrate and the streamer. Therefore, the secondary Bjerknes force aligned the streamers' bubble/water interfaces toward the substrate and confined their motion on the substrate (Fig. 2.8c). The translation of the streamers requires an external magnetic force to align the microstreaming propulsion force along the moving direction. The streamers could slide on a complicated 3D surface due to their low density and the negligible gravitational force. At a frequency of around 1 MHz, speed as fast as 2.6 $\text{mm}\cdot\text{s}^{-1}$ (~ 350 body lengths $\cdot\text{s}^{-1}$) was observed. Aghakhani et al. reported a similar capsule shape design that has a larger size (~ 25 μm) [87]. They added a fin structure to the capsule to break the symmetry of the microstreaming; therefore the streamer could translate even when vertically aligned to a surface. More recently, McNeill et al. improved on the above design by developing a wafer-scale fabrication method to overcome the limitations of resolution and throughput of the 3D printing method [88]. They were able to push the size of the streamer down to 500 nm, corresponding to resonant frequencies over 10 MHz. This improvement makes the acoustic bubble streamers available in submicron size, the same size range as chemical- or light-driven nano-/micromotors. The submicron streamers have the potential to perform many functions within limited space, such as the brain intracerebral microvascular system. In addition, the authors found that the streamers could also be powered by a so-called shape resonant frequency (~ 700 kHz) that is much lower than the bubble's resonant frequency (~ 1.5 MHz). The shape resonance could provide a microstreaming force that is strong enough for propulsion but at the same time weak secondary Bjerknes forces that minimize the streamer/substrate attraction. By switching from the bubble's resonant frequency to the shape resonant frequency, the motion of the

swimmers could be converted from a 2D mode (sliding on a surface) into a 3D mode (swimming in free space), as shown in Fig. 2.8d.

In addition to the efforts of developing bubble streamers of microscopic and nanoscopic sizes, researchers also applied microstreaming for propelling macroscopic objects. Qiu et al. designed functional surfaces ($4\text{ mm} \times 4\text{ mm}$) that contain thousands of microbubbles. The diameter of each bubble on the surface is tens micrometers and the resonant frequency is between 50 and 100 kHz. Significant propulsion force could be generated by simultaneously oscillating all the bubbles on the surface. A macroscale streamer that was assembled from the functional surfaces demonstrated a propulsion force of 0.5 mN (Fig. 2.8e) [89, 92].

The narrow bandwidth of the bubbles' resonant frequency enables users to selectively activate the bubbles in a streamer and achieve real-time manipulation. One example was recently demonstrated by Liu et al. with a structure produced by 3D laser printing [93]. The swimmer ($\sim 1\text{ mm}$) includes gas tubes of three different sizes and the tubes are oriented orthogonally. By activating the three types of bubbles independently or simultaneously, the microstreaming could lift, translate, and rotate the swimmer. A mechanism based on an uneven density distribution was also proposed to restore the swimmer's posture, so the swimmer always stands upright under the effect of gravity and buoyancy. Magnetic steering offers more precise and directional control of the bubble streamers. Ahmed et al. embedded superparamagnetic particles in the swimmer polymer matrix, so that a swimmer could be rotated or oriented into any direction by an external magnetic field [94]. Another approach to achieve magnetic steering is by coating swimmers with a thin paramagnetic film, such as nickel, during the fabrication process [88, 93].

Pickup and transport of cargos with bubble streamers have also been demonstrated [85, 88, 93]. The acoustic pressure required for bubble streamers usually has negligible effects on other objects in the same environment. It allows the streamers to move among the objects, pick up a specific target, and transport it to a new location in 2D. The target could be simply pushed by the propulsion force or dragged by the acoustic attractive force, depending on parameters such as the size of the streamers and the targets, and the acoustic pressure level. For example, Ren et al. demonstrated that microscopic bubble streamer could either push or drag microparticles/cancer cells and independently relocate multiple targets on the substrate.

Practical Considerations

Bubble streamers that operate via cavitation microstreaming offer many advantages over the other types of ultrasound-powered micro-/nanomotors. First, bubble streamers are powered by traveling acoustic waves of low pressure, which allow motors to work regardless of the shapes of fluidic containers and move independently from other objects. Second, bubble streamers of sizes ranging from a few millimeters to a few hundreds of nanometers have been developed. The wide size range enables many applications, such as the removal of tissue samples, single-cell separation, and intracellular drug delivery. Moreover, bubble streamers have demonstrated many unique functionalities by applying acoustic fields alone. By

modulating the acoustic frequency or the acoustic pressure, bubble streamers could change directions, rotate, attract microscopic objects or boundary, transition from 2D to 3D motion, and so on. Many functionalities could be developed with a simple combination of waveform generator and a piezoelectric transducer, without the need of any other equipment.

To move forward, we note that the development of bubble streamers is still at its early stage, and current research mostly focuses on design optimization and the characterization of the basic properties. One key challenge for practical applications is the low reproducibility and short lifetime of the gas bubbles in the streamers. Specifically, it has been reported that streamers from the same fabrication had slightly different resonant frequencies because of the slight but inevitable differences in the bubble size. Moreover, bubbles typically only last for a few hours because of the rectified diffusion (i.e., more gas diffusing into the bubble than out during one cycle of oscillation, leading to bubble growth). More efforts are therefore required for the large-scale production of bubble streamers with controllable bubble sizes and long lifetime. Furthermore, it usually requires sophisticated methods to fabricate 3D bubble streamers, such as nanoscopic 3D printing, which puts a practical limit on both the minimum feature size and throughput. Finally, the biocompatibility of the streamer materials also needs to be considered when it comes to biological applications.

2.3.3 *Flagellar Streamers*

Like the gas/fluid boundary generating cavitation microstreaming, a solid/fluid boundary could also introduce comparatively strong microstreaming when the solid boundary oscillates with a large amplitude. A common observation of this phenomenon is a pair of counter-rotating vortices around an acoustically activated sharp-edge tip [95, 96]. Such streaming was first utilized for fluidic mixing in microfluidics and later applied to the development of acoustic streamers. Under the excitation of acoustic waves, the tip of the sharp edge oscillates like a flagellum of microorganisms but at a much higher frequency, leading to directional microstreaming—and propulsive force in the opposite direction—around the tip. The sharp edges or such structures are often made of materials with low Young's modulus, such as polydimethylsiloxane (PDMS), so that oscillation of a large amplitude can be generated. This type of ultrasound-powered micromotors is referred here as “flagellar streamers.”

Ahmed et al. developed the first acoustic flagellar swimmer that consisted of a flexible polypyrrole flagellum and a metallic head, as shown in Fig. 2.9a, via sequentially depositing layers of materials in an alumina membrane template [97]. The rod-shaped swimmer has a diameter of 0.3 to 0.6 μm and a length of 15 to 20 μm . A traveling acoustic wave was applied to oscillate the polypyrrole flagellum and to generate microstreaming at its end. Consequently, the microstreaming pushed the swimmer to move toward its metal head. A maximum speed of $\sim 60 \mu\text{m}\cdot\text{s}^{-1}$ (3~4

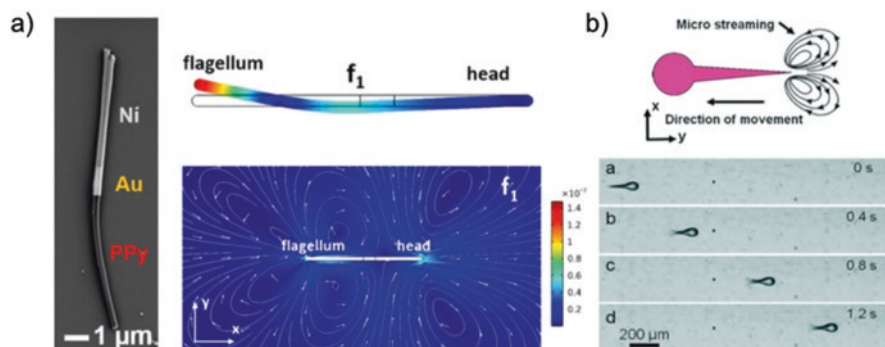


Fig. 2.9 Flagella streamers. (a) SEM image (left) of a nanowire flagellar swimmer. Numerical simulation on the right illustrates the oscillation mode of the polypyrrole tail and the microstreaming pattern associated with the oscillation. Reproduced with permission [97]. Copyright 2016, **American Chemical Society**. (b) Schematic of the sharp-edge flagellar swimmer and the microstreaming pattern near its tail, which propels the swimmer to move away from its tail. Reproduced with permission [98]. Copyright 2017, Royal Society of Chemistry

body lengths \cdot s $^{-1}$) was achieved at \sim 90 kHz and 10 Vpp input voltage. Kaynak et al. later developed a flagellar swimmer of a larger scale with photopolymerizable polymer [98]. The swimmer, around 200 μm long and 60 μm wide, has a round head and a sharp tail. In the presence of an acoustic field (\sim 4.6 kHz), the oscillation of the tail at an amplitude of 20 μm was recorded by a fast camera (Fig. 2.9b), which confirmed the propulsion mechanism of this type of swimmers. At an input voltage of 140 Vpp, a speed of 1200 μm \cdot s $^{-1}$ (6 body lengths \cdot s $^{-1}$) was achieved.

Flagellar streamers can work under traveling acoustic waves and are more stable than bubble streamers. However, the oscillation of the elastic flagella usually requires higher acoustic pressures than bubble streamers to reach the same amplitude of oscillation, because a gas/fluid interface is much easier to deform than a solid/fluid interface. However, the resonant frequency of an acoustically vibrated flagellum is commonly identified through experiments, yet results from numerical simulations did not match the experiments well. In other words, it is difficult to predict the resonant frequency of a flagella design. Deeper understanding of the flagella oscillation mode and optimization of their design are required for practical applications.

In addition to propelling the swimmers themselves, acoustic streaming generated by gas bubbles or sharp edges can also be applied to manipulate passive micro-objects in combination with the acoustic radiation force. For example, Ahmed et al. demonstrated that gas bubbles trapped in a polydimethylsiloxane wall could attract or pump microparticles, depending on the size of the particles [99]. For large objects such as *E. coli*, the strong acoustic radiation force trapped the bacteria on the surface of the bubble, while microstreaming rotated them along an axis that is perpendicular to the acoustic radiation force. Lu et al. used polymer micropillar arrays (5 μm \times 20 μm \times 20 μm) and the microstreaming around the pillars to demonstrate a similar size-dependent particle/cell manipulation [100]. In their experiments,

large cancer cells experienced a secondary acoustic radiation force that is stronger than the drag force induced by acoustic microstreaming. Therefore, the cancer cells were trapped by the pillars. However, the secondary acoustic radiation force is weaker for small-size blood cells, which are then convected by the microstreaming and were not trapped by the pillars. In this way, they could separate cancer cells from blood with high purity ($95 \pm 5\%$). By extending the micropillar design to a boundary, they discovered that the acoustic microstreaming could carry objects to move along the boundary [101]. This kind of acoustic microstreaming near a solid boundary can be exploited precisely to guide micro-objects along a predefined path, as demonstrated very recently by Ma et al. [102]

2.3.4 Acoustic Jets

The last type of ultrasound-powered micro-/nanomotor is based on the use of high-intensity ultrasound to induce acoustic jets as a propulsion mechanism. These types of micro-/nanomotors have great promise for penetrating tissue and cellular barriers due to the high mechanical forces generated under ultrasound-induced internal cavitation. Two main types of fuels have been reported to power these devices, including the use of perfluorocarbon nanoemulsions and gas nanobubbles. For example, the Wang lab pioneered a design of microbullets consisting of $5 \mu\text{m}$ hollow conical tubes loaded with perfluorocarbon emulsions (see Fig. 2.10a for its design). The application of a high-intensity focused ultrasound pulse (single 10-ms-long pulse at 2.25 MHz) vaporized the perfluorocarbon liquid nanoemulsions into gas bubbles, the rapidly expanding volume of which inside the hollow microbullet generated a strong propulsive force that moved the tube like a bullet [103]. We note that this operation mechanism carries a qualitative similarity to microjets that thrust forward by chemically producing gas bubbles from a microtube [104–106]. Based on this “droplet vaporization ignition mechanism,” a “microcannon” was designed to fire loaded nanobullets from a microtube at high speeds in the range of meters per second. The fired nanobullets reportedly penetrated $20 \mu\text{m}$ inside a hydrogel phantom tissue that simulated the mechanical and acoustic properties of human tissues [80]. Moreover, arrays of microcannons were used as a wearable transdermal patch, enabling drug payload delivery into skin that is faster and deeper than passive diffusion [107].

Unlike the above cases where liquid fuels are vaporized by ultrasound waves, there have been reports of microscopic structures that spontaneously trap nanobubbles within a cavity in a way similar to the bubble streamers described in Sect. 2.3.2. For example, polymeric, hydrophobic nano-cups can store stabilized gas nanobubbles inside their cavity as a propellant. A focused ultrasound pulse causes internal cavitation of the entrapped nanobubbles, inducing directional propulsion of the nano-cup (Fig. 2.10b) [108]. The jet-like propulsion of these nano-cups was evaluated in an animal model as a deep tissue penetration delivery platform of oncolytic virus, boasting a 1000-fold increase of gene expression for the vaccine virus over

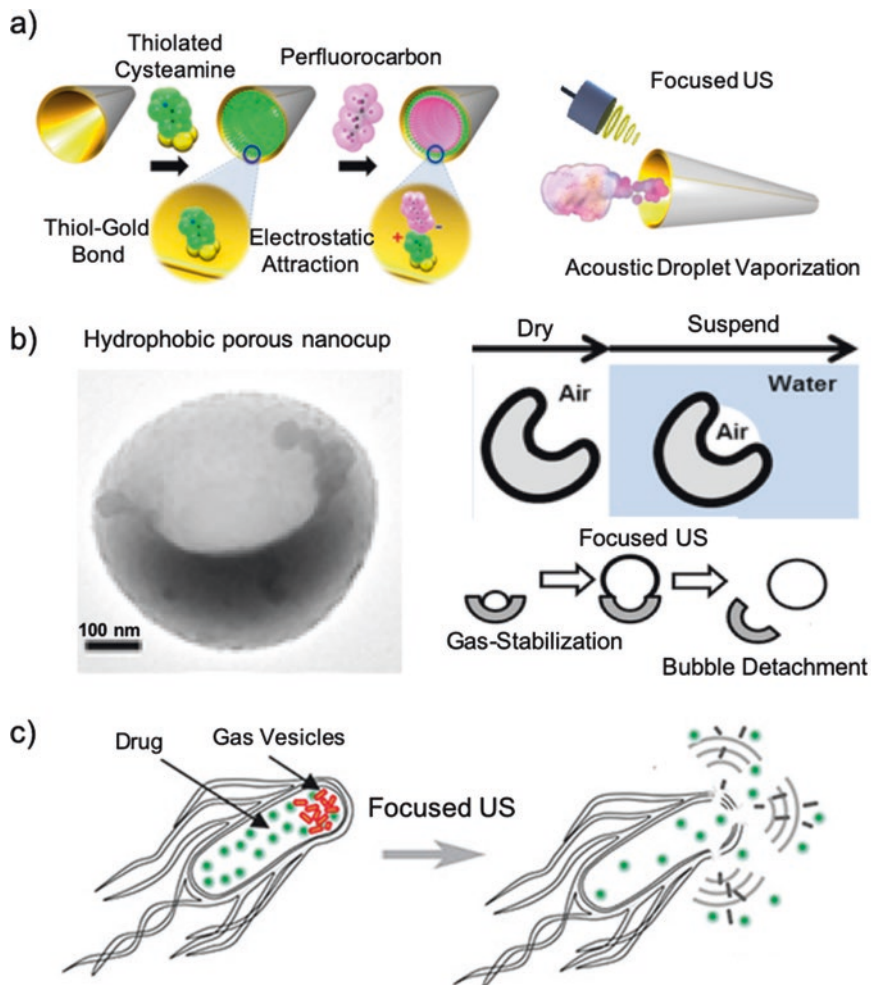


Fig. 2.10 Acoustic jets. (a) Perfluorocarbon-loaded microbullets powered by acoustic droplet vaporization. Reproduced with permission [103]. Copyright 2012, Wiley-VCH. (b) Hydrophobic porous nano-cup powered by nucleating cavitation of trapped gas nanobubbles. Reproduced with permission [108]. Copyright 2015, Wiley-VCH. (c) Genetically encoded bacteria that produce gas vesicles release payload via internal cavitation upon focused ultrasound. Reproduced with permission granted by Prof. Mikhail G. Shapiro [109]

passive diffusion [110]. More recently, genetically engineered bacterium were programmed to produce gas vesicles, which were cavitated using focused ultrasound (3 MHz, 1 MPa) to serve as remotely detonated cell-killing agents (Fig. 2.10c) [109].

The acoustic jets discussed in this section, taking advantage of a streaming/cavitation propulsion mechanism, are powerful and easy to activate. However, they can only be activated once, becoming passive after the fuel is completely vaporized, or the nanobubble detached. The fact that these jets are “single-use” puts a serious

limit on the practical usefulness of acoustic jets in scenarios where repeated activation is essential.

2.4 Conclusion and Future Prospects

In this chapter, we have reviewed the development and state of the art of nanomotors powered by ultrasound of four major types: microrod streamers that move by asymmetric surface microstreaming, bubble streamers powered by microstreaming near an oscillating microbubble, flagella streamers with a solid body that oscillates in ultrasound, and finally acoustic jets that produce jet streaming. Throughout this chapter, one focus is on introducing operating mechanisms, by first giving a general overview of acoustic radiation forces and acoustic streaming and then understanding how streaming is generated for each type of motor and how directional motion is enabled by broken symmetry. A second focus is on the various biomedical capabilities these nanomotors demonstrate. These functionalities include cargo pickup, transport and unloading (both outside a cell and across the cell membrane), cell manipulation (push, pull, rotate), exerting mechanical forces, triggered release of drugs, and magnetic steering, among others.

Beyond listing the preliminary studies and the promises they make, we also pointed out, in each section, specific hurdles that need to be overcome before each type of acoustic nanomotors can find their ways into a clinic. Without going into the detail of the various issues a nanomotor encounters during an *in vivo* operation, a topic already elaborated in a few excellent review articles [111–118], we generalize below a few key scientific and technological challenges that are particularly relevant to micro-/nanomotors powered by ultrasound:

1. Applying ultrasound. The first and foremost requirement of the successful operation of a nanomotor is a proper power source that is biocompatible and effective. Although ultrasound is considered one of the most medically safe power sources, the strategies described in this chapter that power micro-/nanomotors are not necessarily biocompatible. For example, microrod streamers typically require a standing wave to operate, yet it is practically impossible to maintain a standing wave inside human bodies of varying dimensions during the operation of a micro-/nanomotor. Bubble or flagella streamers, on the other hand, only require traveling waves and are in principle easier to implement.
2. Size vs. frequency. A persistent challenge of using nanomotors for biomedicine is a need to identify the best sizes for nanomotors, which have to balance between long retention time in circulation, better chances for cell internalization, and motor performance. This issue is further complicated for ultrasonic nanomotors that move via bubble or body microstreaming (i.e., the first three types), because their sizes determine the resonance frequency, which should ideally match the safe range of diagnostic medical imaging at 1–15 MHz [119]. In other words, a researcher interested in using these motors for biomedical applications needs to

know which sound frequency will be used and keep that number in mind when designing micro-/nanomotors with key features of matching sizes.

3. Interaction with neighbors and the environment. A micro-/nanomotor rarely moves alone in an unbounded space. Rather, it is often surrounded by peers, cells, and other microorganisms and moves in confinements such as blood vessels and extracellular matrix in tissues. The presence of neighbors and a confining environment could significantly affect the speed and directionality of a micro-/nanomotor and even fundamentally change how they behave [120–123]. For example, a microrod streamer is known to be strongly coupled to its neighbor via hydrodynamics, and they together form a spinning chain (see Sect. 2.3.1.1). Similarly, bubble streamers attract and repel with each other via streaming flows. In addition, the presence of strong Bjerknes forces between an oscillating bubble and a nearby solid boundary could make or break a motor (see Sect. 2.3.2.2). A better understanding of these interesting, significant interactions is needed before we can confidently put ultrasonic nanomotors in human bodies.

Despite the challenges and limitations described above, we are optimistic about the prospect of holding an ultrasonic imaging probe to power a micro-/nanomotor that roams blood vessels. This vision is possible, not only because MHz ultrasound is biologically safe, or because of the large number of preliminary studies demonstrating the potential of ultrasound-powered nanomotors in biomedical applications, but also because there is no fundamental reason why this cannot be done. Beyond powering micro-/nanomotors and imaging, ultrasound is also a versatile source of power that enables a range of biomedically relevant effects such as sonodynamic therapy [124], sonoporation [125], and even ultrasonic neurostimulation [126]. We then envision a medical microrobot that moves autonomously, can be imaged from a computer screen, produces therapeutic molecules on cue, breaks through cell membrane, and manipulates cells from outside or from within, all powered by medically safe ultrasound.

Acknowledgment LH and WW are grateful for the financial support by the National Natural Science Foundation of China (11774075), Natural Science Foundation of Guangdong Province (No. 2017B030306005), and the Science Technology and Innovation Program of Shenzhen (JCYJ20190806144807401), as well as past funding from Shenzhen government (KQCX20140521144102503).

References

1. Hagiya, M., Konagaya, A., Kobayashi, S., Saito, H., & Murata, S. (2014). *Accounts of Chemical Research*, 47, 1681–1690.
2. Lancia, F., Ryabchun, A., & Katsonis, N. (2019). *Nature Reviews Chemistry*, 3, 536–551.
3. Fujita, H. (1998). *Proceedings of the IEEE*, 86, 1721–1732.
4. Bryzek, J., Peterson, K., & Mcculley, W. (1994). *IEEE Spectrum*, 31, 20–31.

5. Wang, J. (2013). *Nanomachines: Fundamentals and applications*. Weinheim: Wiley-VCH Verlag GmbH & KGaA.
6. Chen, X., Zhou, C., & Wang, W. (2019). *Chemistry, an Asian Journal*, *14*, 2388–2405.
7. Paxton, W. F., Kistler, K. C., Olmeda, C. C., Sen, A., Angelo, S. K. S., Cao, Y., Mallouk, T. E., Lammert, P. E., & Crespi, V. H. (2004). *Journal of the American Chemical Society*, *126*, 13424–13431.
8. Fournierbidoz, S., Arsenault, A. C., Manners, I., & Ozin, G. A. (2005). *Chemical Communications*, 441–443.
9. Garcíagradilla, V., Sattayasamitsathit, S., Soto, F., Kuralay, F., Yardimci, C., Wiitala, D., Galarnyk, M., & Wang, J. (2014). *Small*, *10*, 4154–4159.
10. Gao, W., Kagan, D., Pak, O. S., Clawson, C., Campuzano, S., Chuluunerdene, E., Shipton, E., Fullerton, E. E., Zhang, L., & Lauga, E. (2012). *Small*, *8*, 460–467.
11. Balasubramanian, S., Kagan, D., Hu, C. J., Campuzano, S., Lobocastanon, M. J., Lim, N., Kang, D. Y., Zimmerman, M., Zhang, L., & Wang, J. (2011). *Angewandte Chemie*, *50*, 4161–4164.
12. Zhang, X., Chen, C., Wu, J., & Ju, H. (2019). *ACS Applied Materials & Interfaces*, *11*, 13581–13588.
13. Zhao, G., Seah, T. H., & Pumera, M. (2011). *Chemistry (Weinheim an der Bergstrasse, Germany)*, *17*, 12020–12026.
14. Soler, L., Magdanz, V., Fomin, V. M., Sanchez, S., & Schmidt, O. G. (2013). *ACS Nano*, *7*, 9611–9620.
15. Gao, W., Feng, X., Pei, A., Gu, Y., Li, J., & Wang, J. (2013). *Nanoscale*, *5*, 4696–4700.
16. Yan, J., Han, M., Zhang, J., Xu, C., Luijten, E., & Granick, S. (2016). *Nature Materials*, *15*, 1095–1099.
17. Gao, W., Pei, A., Feng, X., Hennessy, C., & Wang, J. (2013). *Journal of the American Chemical Society*, *135*, 998–1001.
18. Maggi, C., Simmchen, J., Saglimbeni, F., Katuri, J., Dipalo, M., De Angelis, F., Sanchez, S., & Di Leonardo, R. (2016). *Small*, *12*, 446–451.
19. Wang, W., Lv, X., Moran, J., Duan, S., & Zhou, C. (2020). *Soft Matter*, *16*, 3846–3868.
20. Das, M., Schmidt, C. F., & Murrell, M. (2020). *Soft Matter*, *16*, 7185–7190.
21. Balzani, V., Credi, A., Raymo, F. M., & Stoddart, J. F. (2000). *Angewandte Chemie*, *39*, 3348–3391.
22. Purcell, E. M. (1977). *American Journal of Physics*, *45*, 3–11.
23. Solovev, A. A., Mei, Y., Urena, E. B., Huang, G., & Schmidt, O. G. (2009). *Small*, *5*, 1688–1692.
24. Ma, X., & Sanchez, S. (2015). *Chemical Communications*, *51*, 5467–5470.
25. Moran, J. L., Wheat, P. M., & Posner, J. D. (2010). *Physical Review E*, *81*, 065302.
26. Zhou, C., Zhang, H. P., Tang, J., & Wang, W. (2018). *Langmuir*, *34*, 3289.
27. Ibele, M. E., Mallouk, T. E., & Sen, A. (2009). *Angewandte Chemie*, *48*, 3308–3312.
28. Xu, T., Gao, W., Xu, L., Zhang, X., & Wang, S. (2017). *Advanced Materials*, *29*, 1603250.
29. Chen, X., Jang, B., Ahmed, D., Hu, C., De Marco, C., Hoop, M., Mushtaq, F., Nelson, B. J., & Pane, S. (2018). *Advanced Materials*, *30*, 1705061.
30. Hill, M., & Harris, N. R. (2007). Ultrasonic Particle Manipulation. In S. Hardt & F. Schönfeld (Eds.), *Microfluidic Technologies for Miniaturized Analysis Systems* (pp. 357–392). Boston, MA: Springer US.
31. Wang, W., Castro, L. A., Hoyos, M., & Mallouk, T. E. (2012). *ACS Nano*, *6*, 6122–6132.
32. Bruus, H. (2012). *Lab on a Chip*, *12*, 1014–1021.
33. Sadhal, S. S. (2012). *Lab on a Chip*, *12*, 2292–2300.
34. Jameslighthill, S. (1978). *Journal of Sound and Vibration*, *61*, 391–418.
35. Destgeer, G., Ha, B. H., Park, J., & Sung, H. J. (2016). *Analytical Chemistry*, *88*, 3976–3981.
36. Moo, J. G. S., Mayorga-Martinez, C. C., Wang, H., Teo, W. Z., Tan, B. H., Luong, T. D., Gonzalez-Avila, S. R., Ohl, C.-D., & Pumera, M. (2018). *Advanced Functional Materials*, *28*, 1702618.

37. Leighton, T. G., Walton, A. J., & Pickworth, M. J. W. (1990). *European Journal of Physics*, *11*, 47–50.
38. Memoli, G., Baxter, K. O., Jones, H. G., Mingard, K. P., & Zeqiri, B. (2018). *Micromachines*, *9*.
39. Strutt, J. W. (1884). *Philosophical Transactions of the Royal Society of London*, *175*, 1–21.
40. Riley, N. (2001). *Annual Review of Fluid Mechanics*, *33*, 43–65.
41. Sadhal, S. S. (2012). *Lab on a Chip*, *12*, 2600–2611.
42. Hamilton, M. F., Ilinskii, Y. A., & Zabolotskaya, E. A. (2003). *The Journal of the Acoustical Society of America*, *113*, 153–160.
43. Elder, S. A. (1959). *The Journal of the Acoustical Society of America*, *31*, 54–64.
44. Guo, F., Mao, Z., Chen, Y., Xie, Z., Lata, J. P., Li, P., Ren, L., Liu, J., Yang, J., Dao, M., Suresh, S., & Huang, T. J. (2016). *Proceedings of the National Academy of Sciences of the United States of America*, *113*, 1522–1527.
45. Ahmed, D., Mao, X., Shi, J., Juluri, B. K., & Huang, T. J. (2009). *Lab on a Chip*, *9*, 2738–2741.
46. Zhou, C., Zhao, L., Wei, M., & Wang, W. (2017). *ACS Nano*, *11*, 12668–12676.
47. Paxton, W. F., Sen, A., & Mallouk, T. E. (2005). *Chemistry – A European Journal*, *11*, 6462–6470.
48. Wang, Y., Hernandez, R. M., Bartlett, D. J., Bingham, J. M., Kline, T. R., Ayusman, S., & Mallouk, T. E. (2006). *Langmuir*, *22*, 10451–10456.
49. Lenshof, A., Magnusson, C., & Laurell, T. (2012). *Lab on a Chip*, *12*, 1210–1223.
50. Garciagradilla, V., Orozco, J., Sattayasamitsathit, S., Soto, F., Kuralay, F., Pourazary, A., Katzenberg, A., Gao, W., Shen, Y., & Wang, J. (2013). *ACS Nano*, *7*, 9232–9240.
51. Ahmed, S., Wang, W., Bai, L., Gentekos, D. T., Hoyos, M., & Mallouk, T. E. (2016). *ACS Nano*, *10*, 4763–4769.
52. Nadal, F., & Lauga, E. (2014). *Physics of Fluids*, *26*, 082001.
53. Collis, J. F., Chakraborty, D., & Sader, J. E. (2017). *Journal of Fluid Mechanics*, *825*, 29–48.
54. Nadal, F., & Michelin, S. (2020). *Journal of Fluid Mechanics*, *898*, A10.
55. Soto, F., Wagner, G. L., Garciagradilla, V., Gillespie, K. T., Lakshminpathy, D. R., Karshalev, E., Angell, C., Chen, Y., & Wang, J. (2016). *Nanoscale*, *8*, 17788–17793.
56. Voß, J., & Wittkowski, R. (2020). *Nanoscale Advances*, *2*, 3890–3899.
57. Balk, A. L., Mair, L. O., Mathai, P. P., Patrone, P. N., Wang, W., Ahmed, S., Mallouk, T. E., Liddle, J. A., & Stavis, S. M. (2014). *ACS Nano*, *8*, 8300–8309.
58. Sabrina, S., Tasinkevych, M., Ahmed, S., Brooks, A. M., La Cruz, M. O. D., Mallouk, T. E., & Bishop, K. J. M. (2018). *ACS Nano*, *12*, 2939–2947.
59. Ahmed, S., Wang, W., Mair, L. O., Fraleigh, R. D., Li, S., Castro, L. A., Hoyos, M., Huang, T. J., & Mallouk, T. E. (2013). *Langmuir*, *29*, 16113–16118.
60. Li, Z., Bai, L., Zhou, C., Yan, X., Mair, L., Zhang, A., Zhang, L., & Wang, W. (2017). *Particle & Particle Systems Characterization*, *34*, 1600277.
61. Kiristi, M., Singh, V., De Avila, B. E., Uygun, M., Soto, F., Uygun, D. A., & Wang, J. (2015). *ACS Nano*, *9*, 9252–9259.
62. Uygun, M., Juradosanchez, B., Uygun, D. A., Singh, V., Zhang, L., & Wang, J. (2017). *Nanoscale*, *9*, 18423–18429.
63. Wu, Z., Li, T., Gao, W., Xu, T., Juradosanchez, B., Li, J., Gao, W., He, Q., Zhang, L., & Wang, J. (2015). *Advanced Functional Materials*, *25*, 3881–3887.
64. Esteban-Fernández De vila, B., Angsantikul, P., Ramírez-Herrera, D. E., Soto, F., Teymourian, H., Dehaini, D., Chen, Y., Zhang, L., & Wang, J. (2018). *Science robotics*, *3*, eaat0485.
65. Wang, W., Li, S., Mair, L. O., Ahmed, S., Huang, T. J., & Mallouk, T. E. (2014). *Angewandte Chemie*, *53*, 3201–3204.
66. De Avila, B. E., Martin, A., Soto, F., Lopezramirez, M. A., Campuzano, S., Vasquezmachado, G. M., Gao, W., Zhang, L., & Wang, J. (2015). *ACS Nano*, *9*, 6756–6764.
67. Qualliotine, J. R., Bolat, G., Beltrangastelum, M., De Avila, B. E., Wang, J., & Califano, J. A. (2019). *Otolaryngology-Head and Neck Surgery*, *161*, 194599819866407.
68. De Avila, B. E., Angell, C., Soto, F., Lopezramirez, M. A., Baez, D. F., Xie, S., Wang, J., & Chen, Y. (2016). *ACS Nano*, *10*, 4997–5005.

69. Hansenbruhn, M., De Avila, B. E., Beltrangastelum, M., Zhao, J., Ramirezherrera, D. E., Angsantikul, P., Gothelf, K. V., Zhang, L., & Wang, J. (2018). *Angewandte Chemie*, *57*, 2657–2661.
70. Zhang, F., Zhuang, J., De Avila, B. E., Tang, S., Zhang, Q., Fang, R. H., Zhang, L., & Wang, J. (2019). *ACS Nano*, *13*, 11996–12005.
71. De Avila, B. E., Ramirezherrera, D. E., Campuzano, S., Angsantikul, P., Zhang, L., & Wang, J. (2017). *ACS Nano*, *11*, 5367–5374.
72. Gao, C., Lin, Z., Wang, D., Wu, Z., Xie, H., & He, Q. (2019). *ACS Applied Materials & Interfaces*, *11*, 23392–23400.
73. Wang, D., Gao, C., Wang, W., Sun, M., Guo, B., Xie, H., & He, Q. (2018). *ACS Nano*, *12*, 10212–10220.
74. Ren, L., Wang, W., & Mallouk, T. E. (2018). *Accounts of Chemical Research*, *51*, 1948–1956.
75. Ahmed, S., Gentekos, D. T., Fink, C. A., & Mallouk, T. E. (2014). *ACS Nano*, *8*, 11053–11060.
76. Wang, W., Duan, W., Zhang, Z., Sun, M., Sen, A., & Mallouk, T. E. (2015). *Chemical Communications*, *51*, 1020–1023.
77. Takatori, S. C., De Dier, R., Vermant, J., & Brady, J. F. (2016). *Nature Communications*, *7*, 10694–10694.
78. Ren, L., Zhou, D., Mao, Z., Xu, P., Huang, T. J., & Mallouk, T. E. (2017). *ACS Nano*, *11*, 10591–10598.
79. Xu, T., Soto, F., Gao, W., Garciagradilla, V., Li, J., Zhang, X., & Wang, J. (2014). *Journal of the American Chemical Society*, *136*, 8552–8555.
80. Soto, F., Martin, A., Ibsen, S., Vaidyanathan, M., Garciagradilla, V., Levin, Y., Escarpa, A., Esener, S. C., & Wang, J. (2016). *ACS Nano*, *10*, 1522–1528.
81. Minnaert, M. (1933). *Philosophical Magazine Series 1*, *16*, 235–248.
82. Bertin, N., Spelman, T. A., Stephan, O., Gredy, L., Bouriau, M., Lauga, E., & Marmottant, P. (2015). *Physical Review Applied*, *4*, 064012.
83. Ren, L., Nama, N., McNeill, J. M., Soto, F., Yan, Z., Liu, W., Wang, W., Wang, J., & Mallouk, T. E. (2019). *Science Advances*, *5*.
84. Dijkink, R., Der Dennen, J. P. V., Ohl, C., & Prosperetti, A. (2006). *Journal of Micromechanics and Microengineering*, *16*, 1653–1659.
85. Feng, J., Yuan, J., & Cho, S. K. (2016). *Lab on a Chip*, *16*, 2317–2325.
86. Louf, J., Bertin, N., Dollet, B., Stephan, O., & Marmottant, P. (2018). *Advanced Materials Interfaces*, *5*, 1800425.
87. Aghakhani, A., Yasa, O., Wrede, P., & Sitti, M. (2020). *Proceedings of the National Academy of Sciences of the United States of America*, *117*, 3469–3477.
88. McNeill, J. M., Nama, N., Braxton, J. M., & Mallouk, T. E. (2020). *ACS Nano*, *14*, 7520–7528.
89. Qiu, T., Palagi, S., Mark, A. G., Melde, K., Adams, F., & Fischer, P. (2017). *Advanced Materials Interfaces*, *4*, 1700933.
90. Feng, J., Yuan, J., & Cho, S. K. (2015). *Lab on a Chip*, *15*, 1554–1562.
91. Ahmed, D., Lu, M., Nourhani, A., Lammert, P. E., Stratton, Z., Muddana, H. S., Crespi, V. H., & Huang, T. J. (2015). *Scientific Reports*, *5*, 9744–9744.
92. Qiu, T., Palagi, S., Mark, A. G., Melde, K., Adams, F., & Fischer, P. (2016). *Applied Physics Letters*, *109*, 191602.
93. Liu, F., Cho, S. K. (2019). In *3-D Micro Swimming Drone with Maneuverability*, international conference on micro electro mechanical systems.
94. Ahmed, D., Dillinger, C., Hong, A., & Nelson, B. J. (2017). 1700050. *Advanced materials and technologies*, *2*.
95. Huang, P., Xie, Y., Ahmed, D., Rufo, J., Nama, N., Chen, Y., Chan, C. Y., & Huang, T. J. (2013). *Lab on a Chip*, *13*, 3847–3852.
96. Nama, N., Huang, P., Huang, T. J., & Costanzo, F. (2014). *Lab on a Chip*, *14*, 2824–2836.
97. Ahmed, D., Baasch, T., Jang, B., Pane, S., Dual, J., & Nelson, B. J. (2016). *Nano Letters*, *16*, 4968–4974.

98. Kaynak, M., Ozcelik, A., Nourhani, A., Lammert, P. E., Crespi, V. H., & Huang, T. J. (2017). *Lab on a Chip*, *17*, 395–400.
99. Ahmed, D., Ozcelik, A., Bojanala, N., Nama, N., Upadhyay, A., Chen, Y., Hannarose, W., & Huang, T. J. (2016). *Nature Communications*, *7*, 11085–11085.
100. Lu, X., Martin, A., Soto, F., Angsantikul, P., Li, J., Chen, C., Liang, Y., Hu, J., Zhang, L., & Wang, J. (2018). 1800374. *Advanced materials and technologies*, *4*.
101. Lu, X., Soto, F., Li, J., Li, T., Liang, Y., & Wang, J. (2017). *ACS Applied Materials & Interfaces*, *9*, 38870–38876.
102. Ma, Z., Zhou, Y., Cai, F., Meng, L., Zheng, H., & Ai, Y. (2020). *Lab on a Chip*, *20*.
103. Kagan, D., Benchimol, M. J., Claussen, J. C., Chuluunerdene, E., Esener, S. C., & Wang, J. (2012). *Angewandte Chemie*, *51*, 7519–7522.
104. Xu, B., Zhang, B., Wang, L., Huang, G., & Mei, Y. (2018). *Advanced Functional Materials*, *28*, 1705872.
105. Xu, B., & Mei, Y. (2017). *Science Bulletin*, *62*, 525–527.
106. Li, J., Rozen, I., & Wang, J. (2016). *ACS Nano*, *10*, 5619–5634.
107. Soto, F., Jeerapan, I., Silvalopez, C., Lopezramirez, M. A., Chai, I., Xiaolong, L., Lv, J., Kurniawan, J., Martin, I., & Chakravarthy, K. (2018). *Small*, *14*, 1803266.
108. Kwan, J. J., Myers, R., Coviello, C., Graham, S., Shah, A., Stride, E., Carlisle, R., & Coussios, C. (2015). *Small*, *11*, 5305–5314.
109. Barzion, A., Nourmahnad, A., Mittelstein, D. R., Yoo, S., Malounda, D., Abedi, M., Leegosselin, A., Maresca, D., & Shapiro, M. G. (2019). *bioRxiv*, 620567.
110. Myers, R., Coviello, C., Erbs, P., Foloppe, J., Rowe, C., Kwan, J. J., Crake, C., Finn, S., Jackson, E., & Balloul, J. (2016). *Molecular Therapy*, *24*, 1627–1633.
111. Ghosh, A., Xu, W., Gupta, N., & Gracias, D. H. (2020). *Nano Today*, 100836.
112. Reinisova, L., Hermanova, S., & Pumera, M. (2019). *Nanoscale*, *11*, 6519–6532.
113. Srivastava, S. K., Clergeaud, G., Andresen, T. L., & Boisen, A. (2019). *Advanced Drug Delivery Reviews*, *138*, 41–55.
114. Sitti, M. (2018). *Nature Reviews Materials*, *3*, 74–75.
115. Soto, F., & Chrostowski, R. (2018). *Frontiers in Bioengineering and Biotechnology*, *6*.
116. Sonntag, L., Simmchen, J., & Magdanz, V. (2019). *Molecules*, *24*, 3410.
117. Gao, C., Wang, Y., Ye, Z., Lin, Z., Ma, X., & He, Q. (n/a). *Advanced Materials*, 2000512.
118. Luo, M., Feng, Y., Wang, T., & Guan, J. (2018). *Advanced Functional Materials*, *28*, 1706100.
119. Nelson, T. R., Fowlkes, J. B., Abramowicz, J. S., & Church, C. C. (2009). *Journal of Ultrasound in Medicine*, *28*, 139–150.
120. Patteson, A. E., Gopinath, A., & Arratia, P. E. (2016). *Current Opinion in Colloid and Interface Science*, *21*, 86–96.
121. Bechinger, C., Leonardo, R. D., Lowen, H., Reichhardt, C., Volpe, G., & Volpe, G. (2016). *Reviews of Modern Physics*, *88*, 045006.
122. Katuri, J., Seo, K. D., Kim, D. S., & Sanchez, S. (2016). *Lab on a Chip*, *16*, 1101–1105.
123. Xiao, Z., Wei, M., & Wang, W. (2019). *ACS Applied Materials & Interfaces*, *11*, 6667–6684.
124. Rosenthal, I., Sostaric, J. Z., & Riesz, P. (2004). *Ultrasonics Sonochemistry*, *11*, 349–363.
125. Lentacker, I., De Cock, I., Deckers, R., De Smedt, S. C., & Moonen, C. T. W. (2014). *Advanced Drug Delivery Reviews*, *72*, 49–64.
126. Menz, M. D., Ye, P. P., Firouzi, K., Nikoozadeh, A., Pauly, K. B., Khuriyakub, P., & Baccus, S. A. (2019). *The Journal of Neuroscience*, *39*, 6251–6264.